F. Bariselli, S. Boccelli, T. Magin, A. Frezzotti, A. Hubin
Aerothermodynamic Modelling of Meteor Entry Flows in the Rarefied Regime
in: 12th AIAA/ASME Joint Thermophysics and Heat Transfer Conference, Atlanta, GA, USA, June 25-29, 2018, ISBN: 9781624105524
Paper AIAA 2018-4180 (23 pages)
doi:10.2514/6.2018-4180

Aerothermodynamic modelling of meteor entry flows in the rarefied regime

F. Bariselli *
Vrije Universiteit Brussel, Brussel, Belgium, 1050

S. Boccelli †
Politecnico di Milano, Milano, Italy, 20156

T. Magin ‡
von Karman Institute for Fluid Dynamics, Rhode-Saint-Genèse, Belgium, 1640

A. Frezzotti §
Politecnico di Milano, Milano, Italy, 20156

A. Hubin ¶
Vrije Universiteit Brussel, Brussel, Belgium, 1050

Due to their small size and tremendous speeds, meteoroids often burn up at high altitudes, above 80 km, where the atmosphere is rarefied. Ground radio stations are able to detect the free electrons concentration in the meteoroid wake, which is produced by hyperthermal collisions of the ablated species with the free-stream. The interpretation of radio data, however, currently relies on phenomenological methods, derived under the assumption of free molecular flow, hence, poorly accounts for the dynamics of the vapour, chemistry, and diffusion in the meteor trail. In this work, we aim to provide a detailed description of the flowfield around a meteoroid by means of Direct Simulation Monte Carlo and to obtain the evolution of the free electrons in the meteor wake via an extended trail simulation. An evaporation boundary condition is developed in the framework of an open source DSMC software. The material is assumed to be composed by a mixture of metal oxides which are typically present in ordinary chondritic meteorites. The transport properties of the ablated vapour are computed following the Chapman-Enskog theory and the DSMC phenomenological parameters are retrieved by fitting the collision integrals over a wide range of temperatures. As a last step, chemical and diffusion processes in the trail are computed. Starting from the baseline DSMC solution, our approach marches in time along the precomputed streamlines, calculating chemistry and radial diffusion for metals and free electrons. As study case, the flow around a 1 mm evaporating meteoroid is analysed at different altitudes. A high level of thermal nonequilibrium is appreciated in the head of the meteor, whereas in the trail, after a few diameters, the flow equilibrates. At lower densities, the vapour can travel upstream without interacting much with the incoming jet. On the other hand, at lower altitudes, re-condensation plays a significant role in the stagnation region. Finally, a trail, several meters long and formed by metallic species, generates behind the body. Ionization of sodium turns out to be the dominant process in the production of free electrons, whereas radial diffusion seems to prevail over recombination as depletion mechanism.

I. Introduction

Artificial space systems are not the only objects flying in our sky. About 50 tonnes of small meteoroids enter the terrestrial atmosphere every day [1]. These bodies, from one meter diameter to micron-size grains, originate either

*PhD Candidate, Electrochemical and Surface Engineering Department, federico.bariselli@vki.ac.be
†PhD Candidate, Aerospace Science and Technology Department, stefano.boccelli@polimi.it
‡Associate Professor, Aeronautics and Aerospace Department, thierry.magin@vki.ac.be
§Full Professor, Aerospace Science and Technology Department, aldo.frezzotti@polimi.it
¶Full Professor, Electrochemical and Surface Engineering Department, annick.hubin@vub.be

from sublimating comets or from colliding asteroids. In their rush to the ground, they intersect the atmosphere at hypersonic velocities up to 72 km/s. As a meteoroid interacts with the atmosphere, its surface temperature can reach several thousands of kelvins causing its ablation, i.e. fragmentation, melting and evaporation. The set of phenomena experienced by a meteoroid and the light emitted during the atmospheric entry process are referred to as a "meteor". Due to their small size and tremendous speeds, meteoroids often burn up at high altitudes, above 80 km, where the atmosphere is rarefied. Here, the gas cannot be treated in the continuum assumption and the Navier-Stokes equations usually employed in Gas Dynamics fail [2]. Moreover, as shown in Figure 1, the high energies involved activate coupled physico-chemical phenomena in both the gas and solid phases (strong departure from thermo-chemical equilibrium, radiative heating, ionization and complex gas-surface interactions), making the prediction of these flows an extremely challenging task.

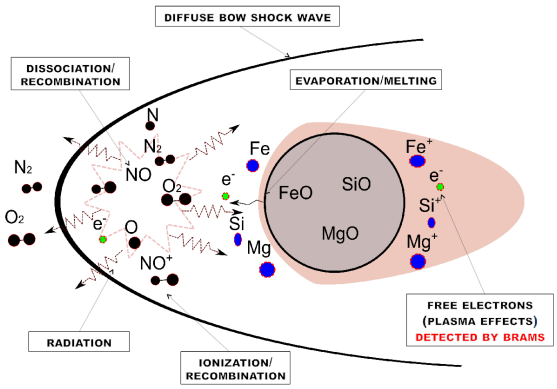

Fig. 1 Schematic of the principal (coupled) physico-chemical phenomena which may occur during meteoroid ablation in the rarefied regime.

Recent efforts have been made by the Belgian Institute for Space Aeronomy to predict velocity, trajectory and mass of meteors. The Belgian RAdio Meteor Stations (BRAMS) experiment consists in a series of receivers spread all over Belgium to collect and standardize the meteor observations [3]. Ground radio stations are able to detect the free electrons concentration in the meteoroid wake, which is directly influenced by ablation mechanisms. Ceplecha estimates that 90% of the electrons production comes from metallic species of meteoric origin [4]. However, the interpretation of radio data currently relies on phenomenological methods, hence, poorly accounts for melting and evaporation of the material, chemistry and diffusion in the meteor trail, and rarefied gas effects.

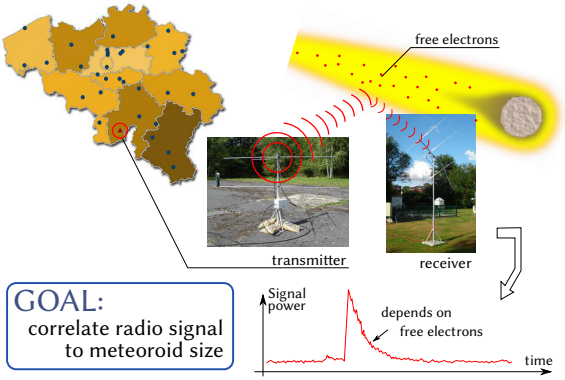

Fig. 2 The Belgian RAdio Meteor Stations (BRAMS) is a network of radio receiving stations using forward scattering techniques to study the meteoroid population [5].

Classical meteor ablation models were derived under the assumption of free molecular flow and evaporation into vacuum. The simplest among these models assumes that the mass loss rate is proportional to the kinetic energy imparted on the meteoroid, with the ablation beginning when the surface of the meteoroid reaches the boiling point [6]. In [7],

Campbell-Brown et al. inferred that this model is not valid for meteoroids of lower densities for which the ablation may start before the boiling temperature is reached. They proposed an ablation model applying the Knudsen-Langmuir formula coupled with the Clausius-Clapeyron relation to compute the equilibrium vapour pressure of the melt-vapour phase transition. In [1], Vondrak et al. adopted a similar approach, with the equilibrium properties of the silicate-vapour system computed by means of a mass balance and mass action software [8].

Boyd [9] was the first to address the problem of the ablation of meteors in the rarefied regime by giving a detailed description of the phenomenon from the flowfield perspective. He treated the meteor material as a single species, i.e. magnesium, using a phenomenological ablation model accounting for evaporation of the metal and assuming a vaporization temperature of 2500 K. No chemical reactions were considered in the gas phase. Preliminary results indicated that a cloud of ablated material surrounds the meteor and that a large high-temperature region in near-thermal equilibrium is present in the meteor's trail. This result is in qualitative agreement with spectral measurements of meteor wakes but is not able to predict quantitatively their composition and ablation rate. A Direct Simulation Monte Carlo (DSMC) [10] approach was also used by Vinkovic [11] to predict the emission of light by very high altitude meteors detected from the ground, not explainable by means of classical ablation theory. The study focused on the sputtering from the meteoroid surface. Strong assumptions were made, such as no distinction between atomic and molecular species in the gas phase. Other physical processes like vaporization, ionization, dissociation, and excitation were not included. A simplified particle-based approach was developed by Stokan et al. [12] to model the space resolved trail luminosity of faint meteors in direct connection to the local number of collisions.

In this work, we aim to provide a detailed description of the flowfield around a meteoroid by means of Direct Simulation Monte Carlo and to obtain, a posteriori, the evolution of the free electrons in the meteor wake via an extended trail simulation. An evaporation boundary condition is developed in the framework of an open source DSMC software [13]. The material is assumed to be composed by a mixture of metal oxides which are typically present in ordinary chondritic meteorites [8]. The transport properties of the ablated vapour are computed in the framework of the Chapman-Enskog theory and the DSMC phenomenological parameters are retrieved by fitting the collision integrals over a wide range of temperatures. As a last step, chemical and diffusion processes in the trail are computed. Starting from the baseline DSMC solution, our approach marches in time along the precomputed streamlines, calculating chemistry and radial diffusion for metals and free electrons.

The paper is structured as follows (see Figure 3). In the next section, an overview of the meteor phenomenon is given, focusing on the physical regimes encountered by the hypersonic body and highlighting the critical limits of currently employed approaches. In Section III we conduct an analysis of the entry trajectory coupled with the material response. This helps to identify those points along the trajectory for which the dynamics of the vapour phase could play a significant role and allow to extract free-stream and wall conditions for the following elaborate analysis. The physical and numerical modelling of the latter and the kinetic interface are introduced in Section IV. Section V describes the procedure employed to obtain the electron concentration in the trail by means of the Lagrangian reactor. Finally, in Section VI, the results are presented.

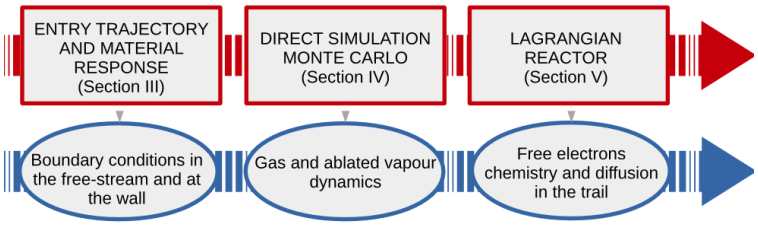

Fig. 3 Flowchart to describe the structure of the paper and the relations between the sections.

II. Overview of the meteor phenomenon

Travelling at geocentric speeds from 12 up to 72 km/s, meteoroids experience hypersonic velocities which can be hundreds of times higher than the speed of sound. The bulk of meteoric material vaporizing in the atmosphere every day is formed by small particles in the range between 5×10^{-5} and 2×10^{-2} m [4]. Radar and radio waves techniques are able to sample meteoroids smaller than optical systems, but big enough to generate a wake of plasma sufficiently intense to be detected. According to Baggaley [14], this corresponds to a rough limit of 10^{-5} m in diameter for meteoroids

travelling at a speed of about 30 km/s. Particles smaller than several hundredths of a millimetre decelerate before reaching the melting temperature. This class of micrometeoroids, for which most of the heat is dissipated by radiation, is not detected neither by radar nor optical techniques and disappear into the atmosphere without the possibility of being tracked.

In the picture of a disintegration process mainly driven by evaporation and mechanical removal, ablation only starts after a pre-heating phase in the thermosphere, in which the surface of the body is heated up to melting conditions. In this phase, since the atmospheric density is extremely low, the meteoroid essentially conserves both its mass and flight velocity. The onset of intense evaporation is computed as the altitude at which the surface starts melting. This altitude is strongly dependent on the velocity and on the dimension of the body, with the smaller and fastest meteoroids being vaporized earlier along their trajectory. A quantitative assessment of the onset of the phenomenon will be performed in Section III, in terms of trajectory analysis.

The role of the dynamics of the gas phase is still unclear. In [6], Bronshten extensively analyses the role of the collisions under subsequent levels of approximation with the aim of studying the effect of the screening due to the reflected or evaporated molecules under different conditions. As a result, he obtains values for the drag, Γ, and heat transfer, Λ, coefficients to be used under the approximations of free molecular flow. Popova et al. [15] stress the importance of taking into account not only air-metal particle collisions, but also metal-metal collisions, due to a large enough number of collisions in the meteor head and vapour clouds. They state that under the condition for which vapour pressure is much higher than the atmospheric pressure, the ablated vapour expands like a hydrodynamic flow into a vacuum. Differently from these approaches, the methodology developed by Stokan [12] disregards the interactions of the evaporated particles among each others.

Figure 4 shows a map of the characteristic conditions encountered by the meteoroids in terms of Knudsen number, $Kn_\infty = \lambda_\infty/D = \lambda_\infty/(2R)$, as a function of the size and the altitude. Let us consider, for example, a 10^{-3} m body falling at 32 km/s, detected by a radar at an altitude of 100 km. The Kn_∞ map suggests that this condition corresponds to free-molecular flight, $Kn_\infty > 10$. However, since the evaporation has already been triggered (the point lays below the line of intensive evaporation), this meteoroid is ablating at a rate, relative to its own mass, which is higher than the 100%. The latter is described by the contours plotted for the normalized ablation rates $\hat{\phi}_e$. In such a condition, the number of collisions per unit time which occur in the vapour cloud is made of two contributions, air-vapour and vapour-vapour interactions, and reads:

$$\dot{N}_{coll} = \dot{N}^{AV}_{coll} + \dot{N}^{VV}_{coll} = n^{eq}_w \sigma R^3 4\pi \frac{1-\sqrt{\kappa}}{\sqrt{\kappa}} \left(n_\infty V_\infty + \frac{n^{eq}_w}{2} \sqrt{\frac{8 k_B T_w}{m\pi}} \right) \tag{1}$$

which has been obtained by integrating the collision frequency of molecules characterized by cross section σ and mass m, over a spherical volume around the object at a distance which spans from its surface to a point in the space in which the vapour number density has decayed by a factor κ. The underlined hypothesis is that the number density of the vapour decays from its value in equilibrium at the surface temperature, $n^{eq}_w(T_w)$, with the square root of the distance to the wall $n^{eq}_w R^2/r^2$. In Figure 4, quantitative values are given for $\kappa = 10^{-3}$. The contribution of air-vapour and vapour-vapour collisions are studied separately. At the onset of evaporation, the contribution of vapour-vapour interactions in thermal equilibrium is found to be comparable, if not more important, to the interactions with the free-stream air molecules, approaching the vapour at hyperthermal velocities. Conversely, in the continuum limit, the latter becomes dominant. By following this approach one can also define a Kn_v based on the collisions experienced by the vapour:

$$Kn_v = \frac{r^2}{2 n^{eq}_w R^3 \sigma} \tag{2}$$

Forming a high density region around the body, the ablated vapours offer a shielding effect in the proximity of the surface, where the gas phase collisions play an important role, thus widening the spectrum of possible regimes which characterize the flowfield (see Figure 5). The vapour seems to reach free-collisions regime within 50 radii from the wall of the meteoroid.

III. Material response along the meteor trajectory

We now consider the thermal response of the meteoroid along its entry trajectory. From the point of view of numerics, this synthetic analysis has the scope of providing relevant boundary conditions for the gas phase simulations, for both the free-stream and the surface. This is important for two reasons. First, the rate of evaporation of metallic

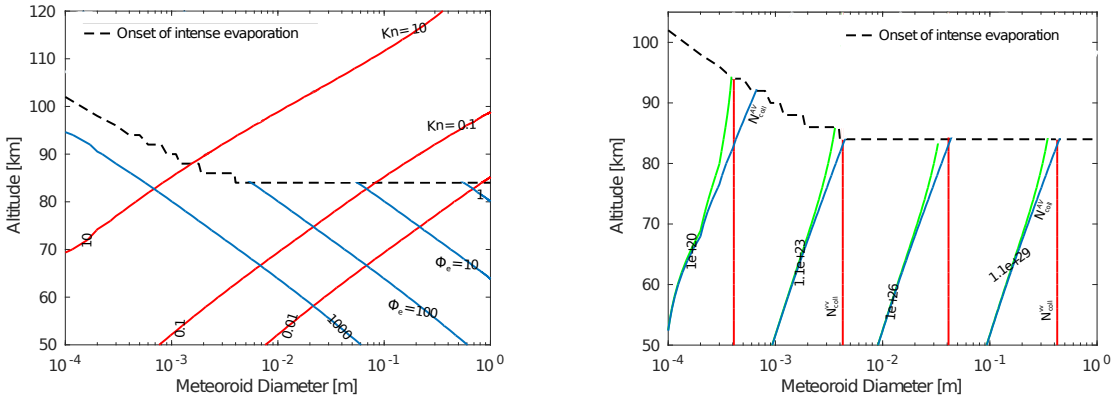

(a) Knudsen number (Kn_∞) —, ablation rate ($\hat{\phi}_e$) —

(b) Number of collisions: total ($\dot{N}_{coll}$) —, vapour-vapour ($\dot{N}^{VV}_{coll}$) —, air-vapour ($\dot{N}^{AV}_{coll}$) —

Fig. 4 On the left, (a), the map of the rarefaction regimes encountered by a meteor is shown by plotting Knudsen number and normalized ablation rate contours in relationship to the diameter of the body and the altitude of the detection. On the right, (b), we show the total number of collisions experienced, per unit time, by the ablated molecules with respect to the diameter of the body and the altitude of the detection. Except for the onset of intense evaporation, air-metal collisions seem to become dominant at lower altitudes and for bigger bodies.

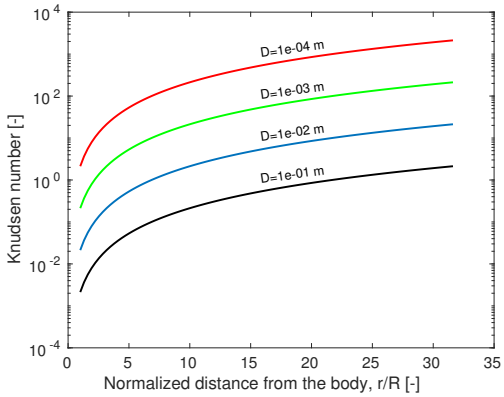

Fig. 5 Evolution of the local Knudsen number (Kn_v) based on the vapour collisions with respect to the distance from the surface of the meteoroid. Starting from a near continuum regime, the vapour reaches a free-collisions condition within 50 radius from the wall.

species, which is the primary source of free electrons, is a strong function of the temperature of the body. Secondly, we are interested in estimating the altitudes at which the evaporation is onset and for which the dynamics of the vapour could play a significant role. Material and trajectory simulations are performed following an explicit procedure: the heat equation (Equation 3) is solved at the local velocity, which in turn is reduced by the effect of drag (Equation 6). For a rapidly tumbling sphere [4], the heat equation reads:

$$\frac{\partial T}{\partial t} = \frac{k}{\rho C_p}\frac{\partial^2 T}{\partial r^2} + \frac{2k}{\rho C_p}\frac{1}{r}\frac{\partial T}{\partial r} \tag{3}$$

The heat equation in this form is obtained by applying a transformation into spherical coordinates $T = T(r,\theta,\varphi,t)$ and dropping the angular dependencies due to the symmetry of the problem.

The vapour-liquid interface is considered as a moving boundary problem as it is described in the next section. The liquid-solid transition is dealt through the *equivalent heat capacity method* [16]. In [17], Dias et al. used this technique

to asses the thickness of the liquid layer which can be taken away by the incoming jet. In this method, only one equation is solved for both the condensed phases without the need of tracking the melting front which is obtained a posteriori. The latent heat of melting, L_m, at the interface is taken into account by assuming a temperature dependency of the heat capacity of the following type:

$$C_p = \begin{cases} C_p^s & T \leq T_m - \Delta T \\ \frac{C_p^s + C_p^l}{2} + \frac{L_m}{2\Delta T} & T_m - \Delta T < T < T_m + \Delta T \\ C_p^l & T \geq T_m + \Delta T \end{cases} \tag{4}$$

where T_m is the melting temperature and ΔT defines the range in which the molten layer and solid coexist, typical feature of melting problems in mixed substances. Equation 3 is solved with the following boundary condition at the vapour-liquid interface:

$$\frac{\Lambda \rho_\infty V_\infty^3}{8} = k \frac{\partial T}{\partial r}\bigg|_w + \epsilon \sigma_S (T_w^4 - T_\infty^4) + \rho L_e v_w \tag{5}$$

representing a surface energy balance where the thermal energy received by the meteoroid (left hand side term) is balanced by the heat conduction, radiative, and vaporization losses on the right hand side. The heat transfer coefficient can be expressed as the product $\alpha_t \alpha_\Lambda$, where the first represents an energy accommodation coefficient, whereas the second represents the probability of a free-stream molecule of reaching the surface and impart its energy to the body instead of being scattered away from the body by colliding with evaporating or reflected particles. The boundary condition 5 is updated along the trajectory by decelerating the body according to the ballistic law:

$$\frac{dV_\infty}{dt} = -\frac{3}{4} \frac{\rho_\infty}{\rho} \frac{\Gamma}{R} V_\infty^2 \tag{6}$$

The recession velocity of the wall, v_w, is obtained by applying a surface mass balance in which the evaporation rate is computed through the Hertz-Knudsen formula:

$$v_w = \alpha_e \frac{n_w^{eq}}{\rho} \sqrt{\frac{m k_B T_w}{2\pi}} \tag{7}$$

which is different from zero only when the surface temperature is close to or above the melting condition. Finally, the change in altitude with time, $H(t)$, is function of the angle of the radiant from the zenith, z_R, as follows:

$$\frac{dH}{dt} = -V_\infty \cos(z_R) \tag{8}$$

A. Numerical method for heat conduction with ablating wall

A finite differences scheme is employed to solve Equation 3. The time integration is performed via an explicit Euler method. The equation is solved in a fixed reference frame, with a boundary (the vapour-liquid interface), which is moved at each time step in agreement with the recession velocity of the wall. At each time step, the mesh is re-generated in order to keep it uniform. If the node at the interface overlaps its neighbour, a node is dropped, so that the space discretization remains nearly constant throughout the simulation. At each time step, the solution previously obtained is re-mapped on the new grid. The effectiveness of this procedure is evaluated by comparing the numerical solution with an exact one for a 1D semi-infinite slab, initially at uniform temperature, T_0, exposed to a step in the surface temperature, T_w, and in the surface recession velocity, v_w. For constant properties, it can be shown that the temperature profile approaches a quasi-steady form [18]:

$$\frac{T - T_0}{T_w - T_0} = \exp\left\{ -\frac{\rho C_p}{k} v_w r \right\} \tag{9}$$

Figure 6 shows the comparison between the computed and exact profiles. For the present conditions, after 100 s, the solution has reached the steady-state and the agreement between the profiles is excellent.

The C_p in the equivalent heat capacity method is approximated through a Gaussian shape to avoid numerical instabilities associated with the singularity. By solving the Stefan problem, an exact solution of the melting problem for

a 1D semi-infinite slab was obtained by Carslaw and Jaeger [18]. We assessed the accuracy of the methodology by comparing the position of the melting front, for which an algebraic equation exists:

$$\frac{T_0 - T_m}{T_w - T_m}\sqrt{\frac{C_p^l}{C_p^s}}\frac{\exp\left\{-C_p^l/C_p^s\,\eta_{ls}^2\right\}}{\mathrm{erfc}\left\{-\sqrt{C_p^l/C_p^s}\,\eta_{ls}\right\}} + \frac{\exp\left\{-\eta_{ls}^2\right\}}{\mathrm{erf}\left\{\eta_{ls}\right\}} - \frac{\sqrt{\pi}\,\eta_{ls}\,L_m}{C_p^l}(T_w - T_m) = 0 \tag{10}$$

where the subscript ls is used to denote the liquid-solid interface and $\eta_{ls} = \frac{r_{ls}}{2\sqrt{k/\rho C_p^l t}}$.

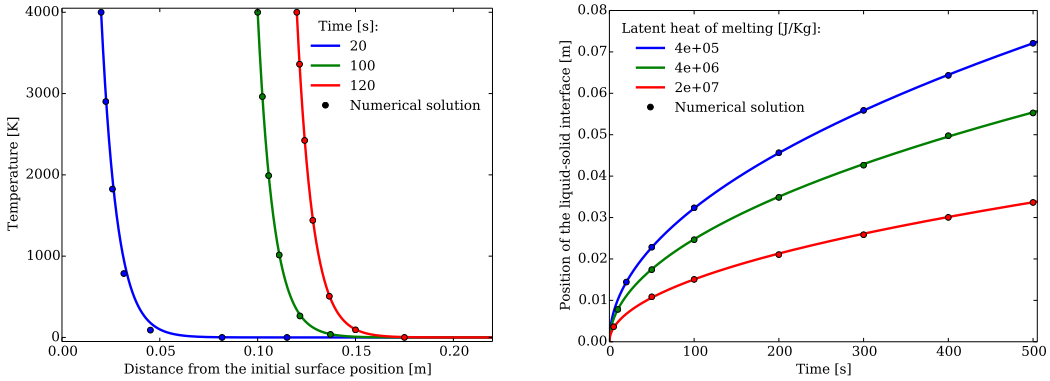

(a) (b)

Fig. 6 Comparison between the exact and numerical temperature profiles for the verification of the receding wall procedure (a) and for the position of the liquid-solid interface in the Stefan problem for the verification of the heat equivalent method (b).

B. Trajectory results

Trajectory simulations have been run for different diameters (1, 2, 5×10^{-3} m) and velocities spanning from 12 to 72 km/s. The simulations have been compared with the data stored in the MSSWG Orbit Database: multi-station video meteor data have been collected over 26 years by the Japanese Meteor Science Seminar Working Group. These data are freely available for download on the International Meteor Organization website [19]. Some data is reported in Figure 7, showing the onset of the meteor phenomenon and its extinction. As a modelling assumption, we assumed that these two points correspond respectively to be beginning and the end of the ablation process. Average values and standard deviations are also reported.

A radiant angle $z_R = 40$ deg, which turns out to be the most probable from the database, has been chosen along with $\Gamma = 1$ and $\Lambda = 0.5$. If the chemical composition of the ordinary chondrites has been widely studied, much less attention has been devoted to characterize their physical properties, especially at high temperatures [20]. In literature, big discrepancies can be found for parameters which turn out to be vital for the predictability of the models (e.g. latent heat and melting temperature). The list of the properties employed in this work to model the material is given in Table 1.

Table 1 Physical properties assumed for the modelling of an ordinary chondrite.

ρ [kg/m^3]	3500	C_p^l [J/kg/K]	1100
k [W/m/K]	3.5	T_m [K]	2000
ϵ [-]	1.0	L_m [J/kg]	4×10^5
C_p^s [J/kg/K]	1050	L_e [J/kg]	4×10^6

Results from our synthetic model appear in the range 2σ of the MSSWG observation. Slower simulated meteors seem to present longer trajectories than the observed ones. A possible explanation could stay in the fact that, for slower

bodies, characterized by lower rates of evaporation, the entrainment of the molten layer by the surrounding gas may represent a significant mechanism of mass loss, which is here not modelled.

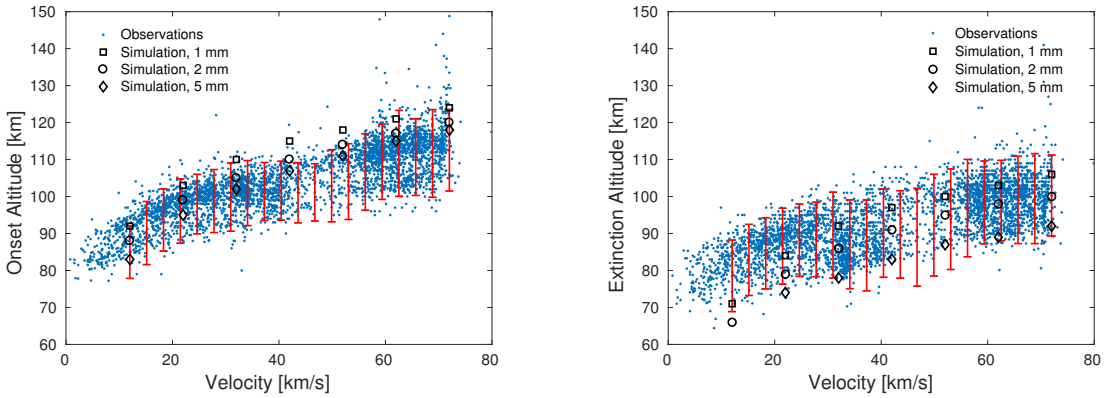

(a) (b)

Fig. 7 Altitude of onset (a) and extinction (b) of the phenomenon from the visual detections stored in the MSSWG Orbit Database [19]. The comparison with the simulated trajectories show a good agreement with the experimental data.

When a meteoroid enters the atmosphere, it starts being heated up very soon. However, down to 200 km, the raise in temperature of the body is generally small. Particles of size 10^{-4} m are characterized by a fast and uniform heating up with negligible temperature gradients between the surface and the core of the body The cooling effect due the re-radiation of the surface is evident for the tinier and slower particles For this condition, the melting temperature is not reached and the body cools down as soon as the meteoroid starts decelerating. The thermal disequilibrium inside the material is enhanced by increasing the velocity and the diameter, as shown in Figure 8.b and 8.c. For bigger bodies (Figure 8.c), the thermal response is delayed and the raise in temperature occurs all of a sudden.

When the surface starts melting, evaporation can commence. From this point of the trajectory on, the energy is dissipated mostly by evaporation and the material does not heat up any more. Only higher heat fluxes (Figure 8.d), encountered at greater velocities, lead the surface temperature to overcome the melting condition. On the other hand, Figure 8.a reveals a condition for which the object stops ablating before being completely disintegrated and glides down to the lower atmosphere layer as it loses momentum.

When small particles start melting, they evolve into molten droplets (see Figure 8.a). Hence, the effect of the flow shear may play an important role, with the mass being lost mainly through mechanical removal. In particles of intermediate size (see Figure 8.a and 8.b), we predict the development of a liquid layer. The latter is not present in the largest and fastest class of bodies under study (see Figure 8.d), where the evaporation front consumes the liquid layer and the two fronts turn out to coincide. Moreover, in this class of meteoroids, heat conduction does not have time to level out the temperature inside the body and the core remains unaffected. It is reasonable to think that this class of meteoroids fragments due to the large thermal stresses at the surface.

IV. Modelling of the flowfield around a meteoroid

As long as the hypothesis of continuum is valid, a hydrodynamic model can be applied. However, under rarefied conditions, the collision rate is too low for the gas to reach local thermodynamic equilibrium, hence, the gas has to be described at the gas kinetic scale, rather than by the Navier-Stokes equation. Such a scale does not allow a fully deterministic approach and a statistical description is more suitable. The function $f_i(\boldsymbol{x},\boldsymbol{\xi}_i,t)$ is defined as the *one-particle velocity distribution function* for the species i and its evolution over time is described by an integro-differential equation: the Boltzmann equation [21], which for a gas mixture can be written as:

$$\frac{\partial f_i}{\partial t} + \boldsymbol{\xi}_i \cdot \frac{\partial f_i}{\partial \boldsymbol{x}} + \frac{\boldsymbol{F}_i}{m_i} \cdot \frac{\partial f_i}{\partial \boldsymbol{\xi}_i} = \sum_{j \in S} \int \left(f_i' f_j' - f_i f_j \right) |\boldsymbol{\xi}_i - \boldsymbol{\xi}_j| \, \sigma_{ij} \, d\omega \, d\boldsymbol{\xi}_j \qquad i \in \mathcal{S} \tag{11}$$

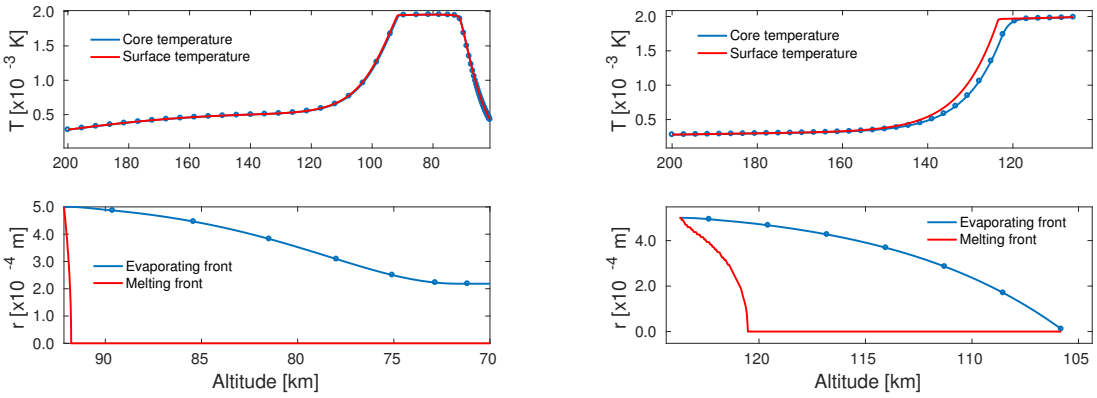

(a) V_∞ = 12 km/s, $D = 10^{-3}$ m

(b) V_∞ = 72 km/s, $D = 10^{-3}$ m

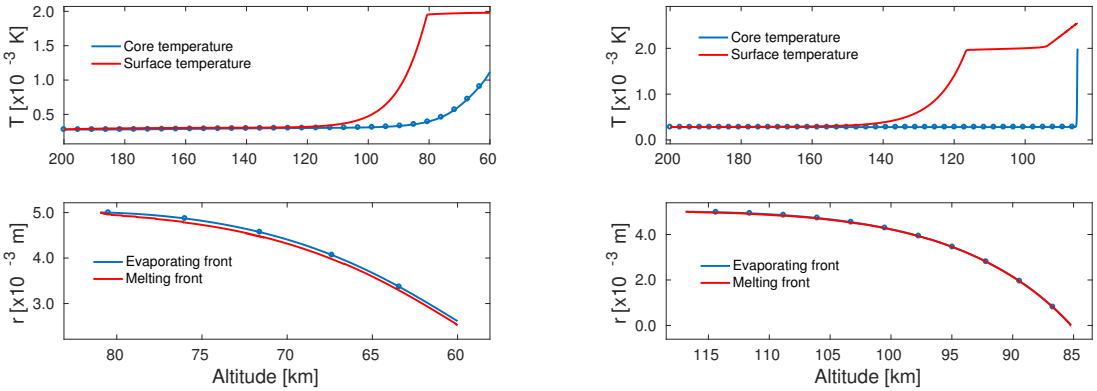

(c) V_∞ = 12 km/s, $D = 10^{-2}$ m

(d) V_∞ = 72 km/s, $D = 10^{-2}$ m

Fig. 8 Temperature and fronts evolution along the trajectories simulated for a range of diameters (D) and velocities (V_∞) typical of the phenomenon. The position of the fronts is computed from the core of the body.

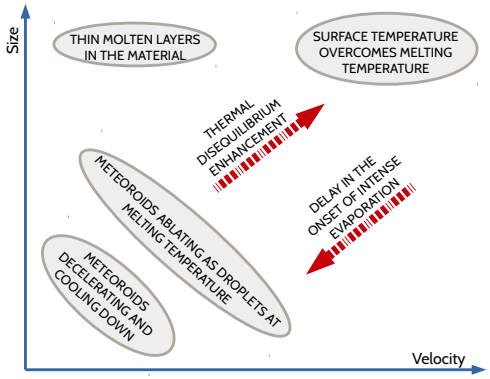

Fig. 9 Map of the phenomena which characterize the material destruction during the meteoroid entry trajectory.

where the left hand side describes the result of macroscopic gradients and external body forces $\boldsymbol{F}_i$ on the velocity distribution function in the physical and velocity space $(\boldsymbol{x},\boldsymbol{\xi}_i)$, whereas the integral at the right hand side models the effect of the binary collisions characterized by cross section σ_{ij}.

First, a kinetic boundary condition needs to be developed for the Boltzmann equation (Section A). Then, the suitable

cross sections need to be extracted and adapted from the available literature (Section B). Finally, since the Direct Simulation Monte Carlo will be the technique adopted for solving the Boltzmann equations, the main DSMC collisional parameters are introduced (Section C).

A. Kinetic boundary condition for evaporation

From a microscopic point of view, the vapour-liquid interface is a finite region whose thickness is 10-20 nominal molecular diameters [22]. At a kinetic scale, its detailed physical structure is neglected and reduced to a surface, Σ, bounding the vapour. The molecular flux of the species i emerging from Σ, which moves at $\boldsymbol{v}_w$ and is characterized by a normal unit vector, $\boldsymbol{n}$, can be modelled by the following inhomogeneous linear boundary condition:

$$f_i[\boldsymbol{\xi}_i - \boldsymbol{v}_w] \cdot \boldsymbol{n} = g_i[\boldsymbol{\xi}_i - \boldsymbol{v}_w] \cdot \boldsymbol{n} + \int_{[\boldsymbol{\xi'}_i - \boldsymbol{v}_w] \cdot \boldsymbol{n} < 0} \mathcal{K}_{B_i}(\boldsymbol{\xi'}_i \rightarrow \boldsymbol{\xi}_i) f_i[\boldsymbol{\xi'}_i - \boldsymbol{v}_w] \cdot \boldsymbol{n} \, d\boldsymbol{\xi'}_i, \;\; [\boldsymbol{\xi}_i - \boldsymbol{v}_w] \cdot \boldsymbol{n} > 0 \;\; i \in \mathcal{S} \quad (12)$$

This comprises 2 contributions: i) the particles coming from the liquid and evaporating into the vapour phase with a half-range Maxwellian. At the equilibrium vapour number density, $n_{w_i}^{eq}$(wall composition, T_w), and temperature, T_w, this distribution can be written as:

$$g_i = \frac{\alpha_{e_i} \, n_{w_i}^{eq}}{(2\pi R_i T_w)^{3/2}} \exp\left\{ - \frac{|\boldsymbol{\xi}_i - \boldsymbol{v}_w|^2}{2 R_i T_w} \right\}, \;\; [\boldsymbol{\xi}_i - \boldsymbol{v}_w] \cdot \boldsymbol{n} > 0 \quad (13)$$

in which R_i is the gas constant defined as k_B/m_i, k_B being the Boltzmann constant and m_i the atomic mass of species i. Departures from equilibrium are taken into account via an evaporation coefficient $0 \leq \alpha_{e_i} \leq 1$; ii) the molecules in the gas phase which, interacting with the wall and not condensing, are scattered back and whose velocity is instantaneously changed from $\boldsymbol{\xi'}_i$ to $\boldsymbol{\xi}_i$ with probability driven by the *scattering kernel*:

$$\mathcal{K}_{B_i}(\boldsymbol{\xi'}_i \rightarrow \boldsymbol{\xi}_i) = (1 - \alpha_{c_i}) \frac{[\boldsymbol{\xi}_i - \boldsymbol{v}_w] \cdot \boldsymbol{n}}{2\pi (R_i T_w)^2} \exp\left\{ - \frac{|\boldsymbol{\xi}_i - \boldsymbol{v}_w|^2}{2 R_i T_w} \right\} \quad (14)$$

In this case, the kernel is written as if the impinging particles were fully thermalized to the temperature of the liquid. The condensation coefficient $0 \leq \alpha_{c_i} \leq 1$ represents the probability to condense for a molecule of the species i.

The determination of the equilibrium properties of the vapour-liquid system is fundamental since they directly influence the kinetic boundary condition through $n_{w_i}^{eq}$. For this purpose, a multi-phase and multi-species equilibrium solver developed by Fegley and Cameron [8] is used. Using a mass action, mass balance algorithm, MAGMA has been widely used to model silicate lavas and has been extensively validated against experimental data [23]. This software assumes evaporation reactions of this type:

$$\mathrm{M}_x\mathrm{O}_y \; (\mathrm{l}) \rightleftharpoons x \; \mathrm{M} \; (\mathrm{g}) + y \; \mathrm{O} \; (\mathrm{g}) \quad (15)$$

where $\mathrm{M}_x\mathrm{O}_y$(l) is an oxide among the ones reported in Table 4 and Equation 15 can be written for a set of change of phase reactions, $\mathcal{R}$. In principle, the thermodynamic equilibrium has to be retrieved by the kinetic approach and, in this sense, the two treatments should be consistent (*detailed balance* condition [24]). A last comment needs to be made on the choice of evaporation and condensation coefficients which are still left as degrees of freedom. Their determination would imply an analysis at the microscopic scale such as the one provided by Molecular Dynamics [22]. This knowledge is still missing for complex systems. For this reason, we assume $\alpha_{e_{\mathrm{M}_i}} = \alpha_{c_{\mathrm{M}_i}} = \alpha_{\mathrm{M}}$ for all the metallic elements which appear in $\mathcal{R}$, and $\alpha_{e_{\mathrm{O}}} = \alpha_{c_{\mathrm{O}}} = \alpha_O$ for oxygen. The two remaining parameters have to be chosen in agreement with the following constraints:

$$\phi_{e_{\mathrm{M}_i}}^{eq} = \phi_{c_{\mathrm{M}_i}}^{eq} \quad i \in \mathcal{R} \quad (16a)$$

$$\phi_{e_{\mathrm{O}}}^{eq} = \phi_{c_{\mathrm{O}}}^{eq} \;\; \Rightarrow \;\; \sum_{i \in \mathcal{R}} \phi_{e_{\mathrm{O}_i}}^{eq} = \phi_{c_{\mathrm{O}}}^{eq} \quad (16b)$$

$$y_i \phi_{e_{\mathrm{M}_i}}^{eq} = x_i \phi_{e_{\mathrm{O}_i}}^{eq} \quad i \in \mathcal{R} \quad (16c)$$

where the first two conditions ensure the possibility of retrieving equilibrium (the rate of evaporation has to be balanced by the rate of adsorption of each species), whereas the third one constraints the molecular fluxes stoichiometrically in agreement with Equation 15.

B. Transport properties of the ablated vapour

Although valuable for a variety of industrial applications, experimental data on transport properties of alkali metal vapours are scarce due to the high temperatures required, low vapour pressures, and corrosive nature [25]. Kinetic theory provides the mathematical framework which allows to link interatomic forces to transport coefficients. As a result of the Chapman-Enskog expansion [26], the binary viscosity coming from the interaction between species i and j reads:

$$\eta_{ij} = \frac{5}{8}\frac{k_B T}{\Omega_{ij}^{(2,2)}} \tag{17}$$

$\Omega_{ij}^{(2,2)}$ represents the so-called *collision integral*, which is obtained by integrating a first time the collision cross section over all the possible impact parameters, b, characterizing the binary collision and, a second time, over the near-equilibrium distribution of relative velocities, g:

$$\Omega_{ij}^{(2,2)} = \sqrt{\frac{2\pi k_B T}{\mu_{ij}}} \int_0^{+\infty} \int_0^{+\infty} e^{-\gamma_{ij}^2} \gamma_{ij}^5 (1 - \cos^2\chi) b db \, d\gamma \tag{18}$$

in which $\gamma_{ij}^2 = \frac{\mu_{ij} g_{ij}^2}{2k_B T}$ is a reduced relative velocity and $\mu_{ij} = \frac{m_i m_j}{m_i + m_j}$ the reduced mass. The scattering angle, $\chi = \chi(b, g, \psi)$, resulting from the dynamic of the binary collision, directly depends on the relevant interatomic potential, ψ. Each type of collision (e.g. neutral-neutral, ion-neutral etc.) would require a different type of potential. However, this procedure quickly becomes cumbersome. In this work, we employ the Lennard-Jones potential:

$$\psi(r_{ij}) = 4\epsilon_{ij}\left[\left(\frac{\bar{\sigma}_{ij}}{r_{ij}}\right)^{12} - \left(\frac{\bar{\sigma}_{ij}}{r_{ij}}\right)^{6}\right] \tag{19}$$

which consists of two parts: a steep repulsive term and smoother attractive term. ϵ_{ij} is the depth of the potential well, $\bar{\sigma}_{ij}$ is the finite distance at which the inter-particle potential is zero and r_{ij} is the distance between the particles.

In order to obtain theoretical viscosity curves for single species vapours, we compute $\Omega_{ii}^{(2,2)}$. For this procedure the Lennard-Jones (6-12) parameters of Table 2 have been employed.

Table 2 Lennard-Jones interatomic potential parameters employed to compute collision integrals for neutral-neutral collisions of metallic species.

Interaction	$\bar{\sigma}$ [A]	ϵ/k_B [K]	Reference
Si-Si	2.910	3036.0	[27]
Mg-Mg	2.926	1614.0	[27]
Al-Al	2.655	2750.0	[27]
Fe-Fe	2.468	7556.0	[28]
Ca-Ca	4.517	50.000	[28]
Na-Na	3.567	1375.0	[27]
K-K	4.250	850.00	[28]

In Figure 10, a comparison between our prediction and a few sets of available experimental results [29–32] is provided. Differences between theory and experiments may come from the presence of molecules or ions in the vapours. Important uncertainty on the potential parameters are likely to be present and one could also argue that the Lennard-Jones potential (6-12) does not apply to alkali metals such as potassium. In [25], Ghatee states that it fails in the prediction of transport properties of K, Rb, and Cs metals vapour especially in the low temperature range. Nonetheless, in our study, the comparison turns out to be fair, with Na's viscosity which lays between the two sets of data and the K's extremely close. The comparison for K's conductivity, computed as:

$$\lambda_{ii} = \frac{15}{4}\frac{k_B}{m_i}\eta_{ii} \tag{20}$$

is even excellent.

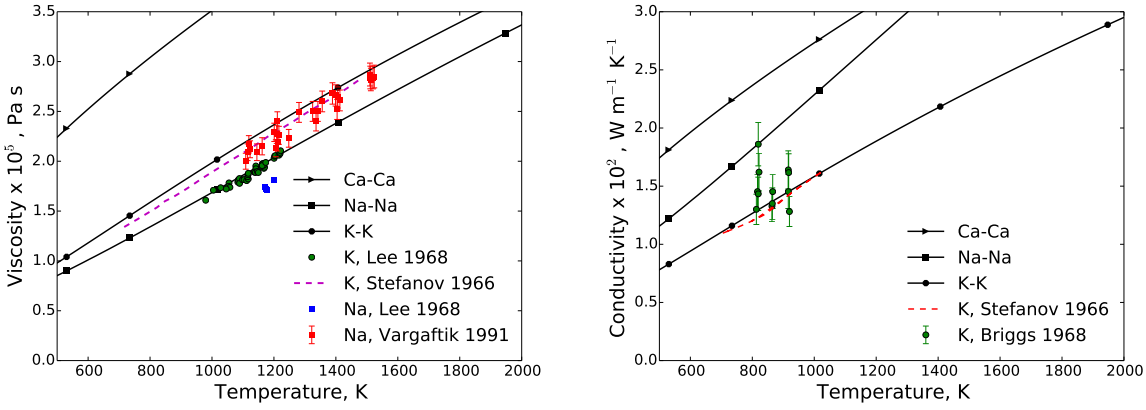

(a) (b)

Fig. 10 Shear viscosity (a) and thermal conductivity (b) for some alkali atoms and comparison with available experimental data. Ca, which is not an alkali metal, is kept as a reference.

C. Numerical method: Direct Simulation Monte Carlo

Direct Simulation Monte Carlo is a particle-based method for the numerical solution of the Boltzmann equation [10]. This technique has been widely used in the aerospace community over the last 50 years to simulate hypersonic flows [33, 34] with a high degree of thermo-chemical nonequilibrium. The trajectories of a representative number of molecules are simulated in the physical space: the particle advection phase is treated deterministically integrating in time the ballistic trajectories, whereas the collision integral of Equation 11 is solved by means of Monte Carlo stochastic evaluation of the collision pairs. The SPARTA software [13] is used here. Developed at the Sandia Labs, this is an open-source DSMC tool and its object-oriented philosophy enables extensions and its usage as a library.

The internal energy exchanges are modelled according to the classical Larsen-Borgnakke phenomenological model [10]. Chemical reactions from the NASA Air-11 mixture [35] are accounted through the Total Collision Energy (TCE) method [10]. This method consists of assuming an analytic form for the collision-dependent reaction cross-section. When averaging this cross-section over a Maxwellian velocity distribution, it is possible to equate it to known rate coefficients in Arrhenius form. Strictly speaking this method is exact only under the assumption of thermal equilibrium. Free electrons are treated under the ambipolar assumption which is the standard approximation for low density plasmas and leads to charge neutrality [36, 37].

In DSMC, the transport properties are the natural result of the simulated binary collisions. DSMC relies on a phenomenological potential to make molecules interact. Although apparently simplistic, these models are able to reproduce to some extent the most salient physics of the collision process, with the advantage of being computationally cheap. These models are discussed by Bird and the reader can refer to his book. In the Variable Soft Sphere (VSS) model, molecules are approximated as rigid spheres of diameter d, which depends on the relative velocity of the impact. The total cross section is written as:

$$\sigma_T^{VSS} = \pi d_{ref}^2 \left(\frac{g_{ref}}{g} \right)^{2\omega - 1} \tag{21}$$

The quantities d_{ref} and g_{ref} are reference values evaluated at a reference temperature T_{ref}, whereas ω is the temperature exponent which allows the variation of the particle diameter with temperature. In this way, molecules with higher impact energies spend less time interacting on the potential energy surface. In the VSS model, the scattering law reads:

$$\chi^{VSS} = 2\cos^{-1}\left[\left(\frac{b}{d} \right)^{1/\alpha} \right] \tag{22}$$

which allows to model anisotropic scattering events through the exponent α (where $\alpha = 1$ corresponds to an isotropic scattering law). It is well known that such a model fails in the attempt of capturing diffusion processes in mixtures of gases and that the anisotropy of neutral-charged collisions in weakly ionized gases is not accurately described [38]. In SPARTA, the collision parameters are obtained by averaging the properties of the collision partners: $d_{ref_{ij}} =$

$(d_{ref_i} + d_{ref_j})/2$, $\omega_{ij} = (\omega_i + \omega_j)/2$, $\alpha_{ij} = (\alpha_i + \alpha_j)/2$. The collision integrals of Equation 18, $\Omega_{ii}^{(2,2)}$ can be expressed as function of the VSS model parameters:

$$\Omega_{ii}^{(2,2)}\Big|_{VSS} = \frac{4\alpha_i}{(\alpha_i+1)(\alpha_i+2)} \frac{\pi d_{ref_i}^2}{2} \sqrt{\frac{k_B T}{2\pi\mu_{ii}}} \left(\frac{T_{ref_i}}{T}\right)^{\omega_i - 1/2} \frac{\Gamma(9/2-\omega_i)}{\Gamma(5/2-\omega_i)} \tag{23}$$

Starting from Equation 23, an independent least squares fitting is performed to obtain the VSS parameters for each collision pair (see Figure 11) $T_{ref} = 1000$ K has been chosen as reference temperature. The fitting has been done in such a way that the error is minimized in the range of temperatures between 800 K and 4000 K. This is indeed the range of temperature of the metallic species, which are emitted from the surface with temperatures in the vaporization range. Table 3 reports the VSS parameters obtained through this procedure.

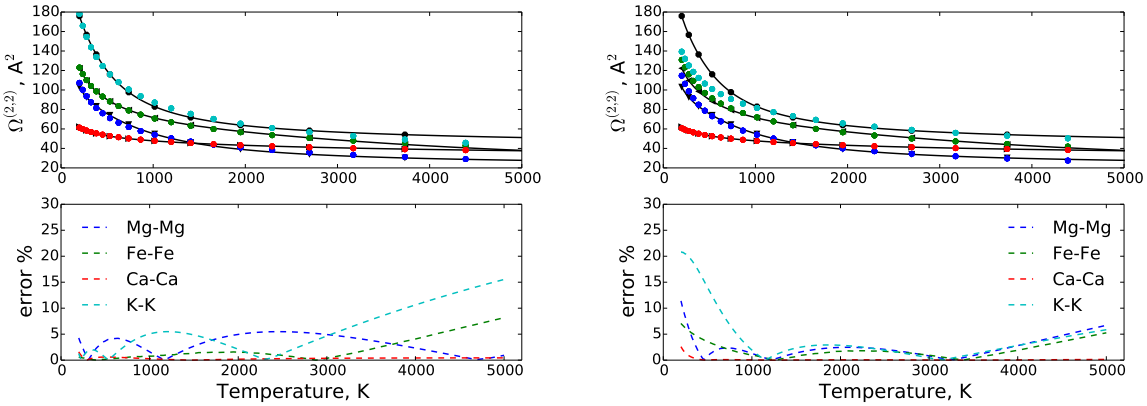

Fig. 11 Fitting procedure of the VSS collision integrals with their exact formulation for some metallic atoms. Two possible choices are proposed, (a) to minimize the error between 200 and 5000 K or to (b) minimize the error between 800 and 4000 K.

Table 3 Variable Soft Sphere (VSS) parameters obtained by fitting the collision integral $\Omega_{ii}^{(2,2)}$ for T_{ref} = 1000 K. This procedure is equivalent to tuning VSS parameters to experimental viscosity data. The average fitting error is reported for the range between 800 K and 4000 K.

Interaction	d_{ref} [A]	ω [-]	α [-]	Error % [-]
Si-Si	5.991	0.985	1.293	0.99
Mg-Mg	5.091	0.962	1.370	1.53
Al-Al	5.362	0.991	1.377	0.77
Fe-Fe	5.605	0.869	1.225	1.09
Ca-Ca	4.117	0.648	1.170	0.04
Na-Na	5.865	0.934	1.250	1.86
K-K	5.862	0.830	1.177	2.04

V. Modelling of the chemical reacting and diffusing trail

Modelling the meteor trail offers a set of additional challenges. The most important one concerns its large extent, which can reach several hundreds of metres. A numerical simulation of such a thin and elongated geometry would not

be feasible using standard DSMC tools, since the computational resources would be easily outnumbered. However, by exploiting the properties of the trail flow, an ad hoc numerical solver can be developed. The result is a lightweight tool able to produce detailed maps of chemicals and free electrons along the meteor trail.

The wake can be divided in two regions: a near region, where the density and velocity change considerably. The temperature starts decreasing and recombination reactions start playing a role; a far region, where velocity, density and temperature have reached the free-stream values. Here, chemistry is typically still out of equilibrium and, together with diffusion, drives the evolution of the trail [39, 40]. A schematic is provided in Figure 12.

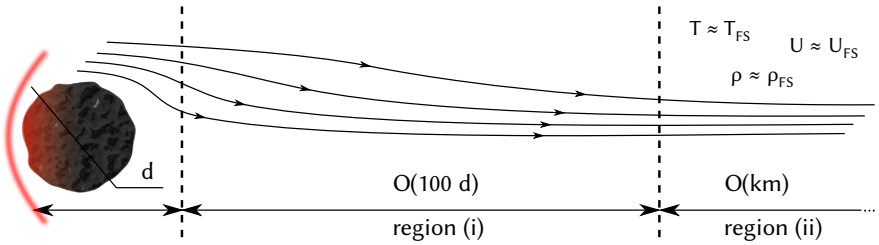

Fig. 12 Fluid dynamic regions in a meteoroid wake. Drawing out of scale.

We can take advantage of two trail properties. First, due to its elongated shape, gradients of fluid and chemical quantities along the trail are mainly directed in the radial direction. Since gradients are the main driving forces for mass and energy diffusion processes, this implies that radial diffusion dominates over the streamwise one. The governing equations thus become parabolic and a lightweight marching numerical scheme can be employed. Second, despite the high degree of rarefaction, the flow thermalizes as the trail develops. Some numerical experiments have been performed to assess the amount of nonequilibrium, around meteoroids, extracting the velocity distribution function (VDF) from DSMC simulations. Figure 13 and 14 show the results for a 1 cm meteoroid, flying at 20 km/s. The shock region (Figure 13) shows a very high degree of nonequilibrium: the free stream particles (seen as a sharp peak at 20 km/s) is easily distinguished from the scattered molecules (with a Maxwellian distribution characterized by negative velocities). The effect of collisions is slightly visible, populating a region that connects the two families of particles.

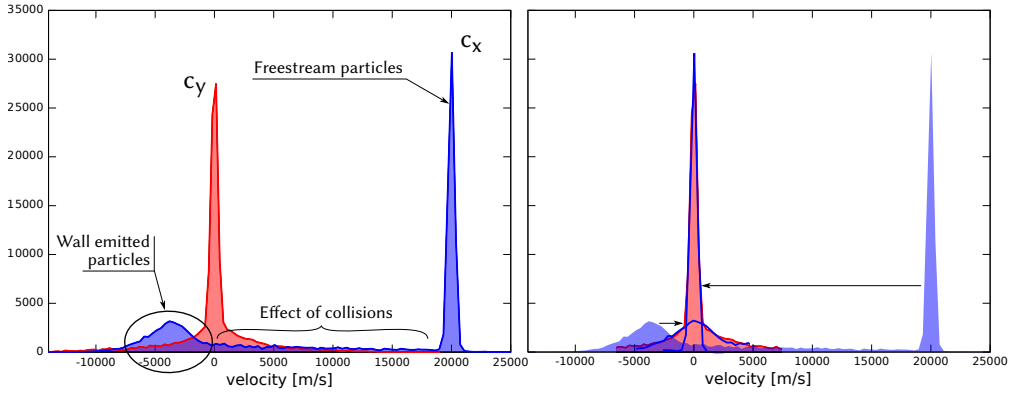

Fig. 13 Velocity distribution function (VDF) in the shock layer for the axial (ξ_x) and radial (ξ_y) velocities. Two populations are visible in the axial VDF: the free-stream and the wall-scattered molecules. The same populations, with zero average velocity but the same temperature, can be distinguished from the radial VDF.

Despite the shock region, the trail (Figure 14) thermalizes after only a few diameters from the body. The temperature anisotropy is quickly relaxed and the bimodal shape of the radial VDF, characteristic of rarefied axisymmetric configurations, fills. This property allows to employ in the trail diffusion models based on gradients of thermodynamic quantities, such as the Fourier's law and multicomponent mass diffusion.

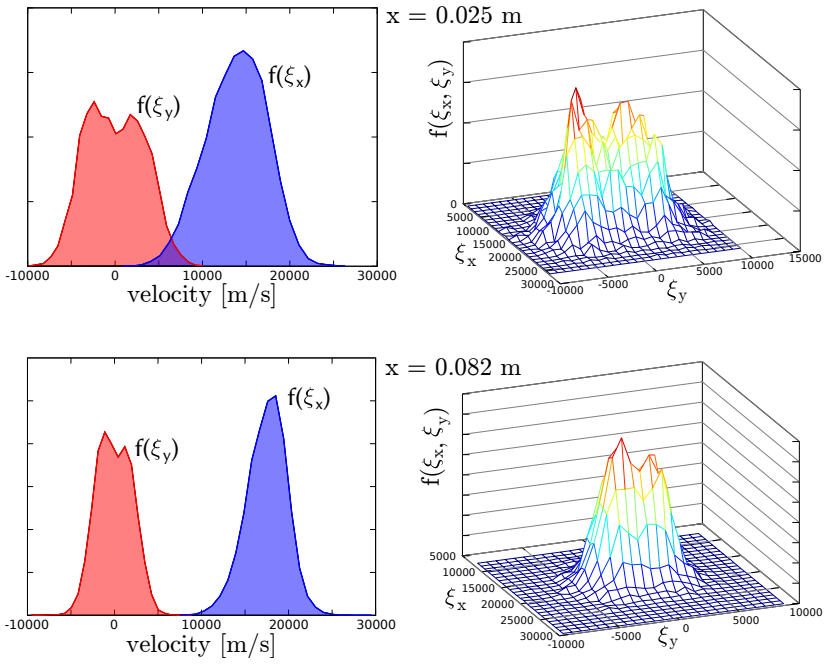

Fig. 14 VDF at two locations in the trail for the axial (ξ_x) and radial (ξ_y) velocity components. The sampling is performed at 0.025 and 0.085 m after the body.

A. Governing equations for the trail

Independently from the degree of rarefaction of a reacting flow, one can always write a set of species mass, momentum, and energy conservation equations at the macroscopic level [41, 42]:

$$\partial_t \rho_i + \boldsymbol{\nabla} \cdot (\rho_i \boldsymbol{u}) + \boldsymbol{\nabla} \cdot (\rho_i \boldsymbol{V}_i^d) = \dot{\omega}_i \quad i \in \mathcal{S} \tag{24a}$$

$$\partial_t (\rho \boldsymbol{u}) + \boldsymbol{\nabla} \cdot (\rho \boldsymbol{u} \otimes \boldsymbol{u}) + \boldsymbol{\nabla} \cdot \boldsymbol{\Pi} = 0 \tag{24b}$$

$$\partial_t (\rho e) + \boldsymbol{\nabla} \cdot (\rho e \boldsymbol{u}) + \boldsymbol{\nabla} \cdot \boldsymbol{q} + \boldsymbol{\Pi} : \boldsymbol{\nabla u} = 0 \tag{24c}$$

In these equations, ρ_i represents the density of the i-th species, $\boldsymbol{u}$ the hydrodynamic velocity, $\dot{\omega}_i$ the chemical production rates, and $\boldsymbol{V}_i^d$ the diffusion velocities. We employ only one momentum equation for the whole mixture (*single-fluid* model), where $\boldsymbol{\Pi}$ is the stress tensor, and a single equation for the mixture thermal energy e (*single-temperature* model), where $\boldsymbol{q}$ is the heat flux due to thermal conduction and mass diffusion.

In the quasi-Maxwellian trail (see what previously discussed in this Section V and Figure 14), expressions for the diffusive fluxes $\rho_i \boldsymbol{V}_i^d$, $\boldsymbol{\Pi}$ and $\boldsymbol{q}$ can be obtained from the Chapman-Enskog theory [43]. Diffusion velocities are written as a linear combination of the gradients of species concentration X_i, through the multicomponent diffusion matrix $\mathcal{D}_{ij}$, and the (ambipolar) electric field $\boldsymbol{E}$:

$$\boldsymbol{V}_i^d = -\sum_{j \in \mathcal{S}} \mathcal{D}_{ij} \boldsymbol{\nabla} X_j + \mathcal{K}_i \boldsymbol{E} \quad i \in \mathcal{S} \tag{25}$$

For simplicity, the stress tensor will be assumed isotropic in this work: $\boldsymbol{\Pi} \equiv P\boldsymbol{I}$. Heat fluxes include conduction, modelled with Fourier's law, and diffusion of energy:

$$\boldsymbol{q} = -k \boldsymbol{\nabla} T + \sum_{i \in \mathcal{S}} \rho_i e_i \boldsymbol{V}_i^d \tag{26}$$

where the temperature gradients $\boldsymbol{\nabla} T$ and the heat conduction coefficient k appear. Diffusion velocities transport the species energy e_i.

B. Numerical method: a Lagrangian tool for the trail (re)computation

We assume that chemistry and the velocity field are partially decoupled: the idea is that velocity and density obtained with a simple chemical model do not change much if minor species are added a posteriori into the problem. This thermochemical refinement approach was verified in a number of test cases by the authors in [44]. Moreover, some preliminary simulations on non-ablating meteoroids show that this is actually the case. First, a baseline DSMC solution is imported and the streamlines are extracted. Then, the set of mass and energy equations are solved along such streamlines: the velocity and density fields are taken from the baseline simulation and are not recomputed; the initial species concentration and temperature are picked from the beginning of the streamlines. More chemical species and reactions can be included in the initial problem. The governing equations are obtained by recasting Equations 24 into Lagrangian form along the streamlines. This implies reshaping the equations to let emerge the material derivative: $\boldsymbol{u} \cdot \boldsymbol{\nabla} \equiv U \mathrm{d}/\mathrm{d}s$, where s is the streamline curvilinear abscissa. After introducing the mass fractions $Y_i = \rho_i/\rho$, the mass equation of the i-th species reads:

$$\frac{\mathrm{d}Y_i}{\mathrm{d}s} = \frac{\dot{\omega}_i - \boldsymbol{\nabla} \cdot \left(\rho_i \boldsymbol{V}_i^d\right)}{\rho U} \tag{27}$$

where U is the hydrodynamic velocity module. The same can be done for the energy equation, from which a temperature equation is obtained:

$$\frac{\mathrm{d}T}{\mathrm{d}s} = \left[Q - \frac{1}{2}\frac{\mathrm{d}U^2}{\mathrm{d}s} - \sum_{i \in \mathcal{S}} h_i \frac{\mathrm{d}Y_i}{\mathrm{d}s}\right] \Big/ \left[\sum_{i \in \mathcal{S}} Y_i c_{p,i}\right] \tag{28}$$

where $Q = \mathrm{d}H/\mathrm{d}s$ is the variation of enthalpy along the streamline and can be expressed, neglecting viscous stresses, as $Q = -\boldsymbol{\nabla} \cdot \boldsymbol{q}/\rho U$, and $\boldsymbol{q}$ can be evaluated with Equation 26. Note that since the velocity is entirely taken from the baseline simulation, there is no need in solving a momentum equation. Also, since the density comes directly from the velocity field through the mass equation, there is no need of solving a global mass equation, and it is sufficient to import the density from the baseline solution. Note that the streamlines are coupled through the diffusion fluxes, which are supposed to be purely radial, in the slender-trail approximation. At every position along the trail, the Equations 27 and 28 are discretized radially using a finite volumes scheme. Thermodynamic and transport properties, in addition to finite rate chemistry, are obtained by means of the Mutation++ library [45]. The resulting system is integrated along the axis of symmetry, using a Rosenbrock-4 or Runge-Kutta numerical procedure. Note that a conversion between a derivative along the i-th streamline s_i and a derivative along the symmetry axis x is simply obtained by taking the local streamline slope α_i into account:

$$\mathrm{d}x = \cos\alpha_i \, \mathrm{d}s_i \quad \Longrightarrow \quad \frac{\mathrm{d}\bullet}{\mathrm{d}x} = \frac{1}{\cos\alpha_i}\frac{\mathrm{d}\bullet}{\mathrm{d}s_i} \tag{29}$$

The computational requirement of this whole procedure is clearly much smaller than running a DSMC or full CFD trail simulation and can be employed thanks to the parabolic nature of the governing equations. The spared resources can be devoted to employing much more complicated chemical models into the problem, with a large number of minor species.

The energy diffusion implementation is checked against the simple analytical result provided by the Laplace equation for the temperature field, whose solution is the error function $\mathrm{erf}(\eta)$. A set of parallel streamlines with uniform velocity is assigned as baseline solution and the temperature is set at a slightly higher value on the bottoming streamline. The flow evolves and exchanges energy, in analogy to a boundary layer. The space position is then remapped to a Lagrangian time and comparison can be compared to the analytical solution. Results show an accurate reproduction of the analytical result (Figure 15.a). The test case is successfully repeated for mass diffusion, where small perturbations in the concentration can be shown to follow the same diffusion equation. An additional verification is performed against a DSMC simulation, for a non-ablating meteoroid. In this test, the Lagrangian tool recomputes the diffusion of mass and energy with the models 25 and 26, and uses the same set of chemical reactions as the DSMC. The results are compared at the exit of the domain in terms of free electrons concentration, in Figure 15.b. Not only the recomputed solution follows well the DSMC baseline: the statistical noise that in DSMC strongly affects minor species is seen to be damped out.

VI. Results

More than the 90% of meteorites collected on the ground is represented by ordinary chondrites. Similarly to magmatic rocks such as basalt, these meteorites are composed by a mixture of metal oxides with a composition close to

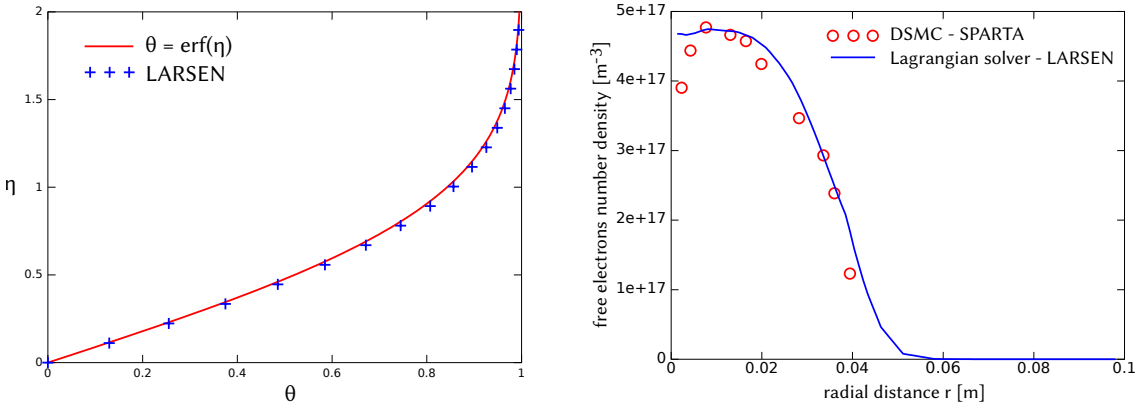

(a) (b)

Fig. 15 On the left (a), the diffusion scheme implemented in the Lagrangian reactor computation (LARSEN) is verified against the analytical solution. On the right (b), the number density of free electrons at the exit of the computational domain is computed to asses the quality of the decoupled approach.

the one reported in Table 4, extracted directly from [1]. For the purpose of our modelling, from here on, this will be considered as the meteoroid prototype.

Table 4 Chemical composition chosen as reference for the modelling of an ordinary chondrite [1].

Oxide	Mass %	Oxide	Mass %
SiO_2	34.0	CaO	1.9
MgO	24.2	Na_2O	1.0
FeO	36.3	K_2O	0.1
Al_2O_3	2.5	TiO_2	0.01

According to Figure 7, the altitude of detection roughly spans from 80 to 120 km. In this work, we investigate the flow around a 1 mm meteoroid, flying at 32 km/s, at three different altitudes: 80, 100, and 120 km. The surface temperature is set to 2000 K. This value is chosen in agreement with the results of Section B, in which, after the onset of the evaporation, the wall temperature reveals a plateau not far from the melting condition. At this temperature, the main contribution to the equilibrium vapour pressure is given by the volatile species, Na and O_2 (see Figure 16.a). This results in an injection rate which is dominated by Na_2O, whereas Fe, Mg, and Si are present as trace elements. In DSMC, each simulated particle corresponds to a large number of real molecules, hence, it is difficult to accurately track minor species which are affected by noise and statistical error. Other species, such as Al, Ca, and K, which are predicted to be in even lower fractions, are excluded from the simulation.

As shown by Figure 16.b, sodium contribution to the electron production turns out to be dominant. As suggested in [46], besides associative and electron impact ionization of air species, a set of reactions which models the direct impact ionization process

$$M + N_2 \rightarrow M^+ + N_2 + e^- \tag{30}$$

has been added to the Park's mechanism. In Reaction 30, M represents a metallic atom, whereas N_2 can be substituted with any other species present in the flow. Provided the fact that the ionization potentials of metallic species, e.g. 5.14 eV for sodium, are lower than the energy required to break the bond of the nitrogen molecule (9.79 eV), in this work, we employ preliminary rates which are based on the Park's rate for N_2 dissociation.

In Figure 17.a, we can see a diffused bow shock developing in front of the body. The shock wave becomes more and more diffuse as the free-stream density decreases, and the bow shape, well visible at 80 km, gradually disappears. As result of the thermal nonequilibrium, tremendous temperatures are computed. From the DSMC point of view, these temperatures are related to the width of the overall VDF which comes from the blending of the distributions of the

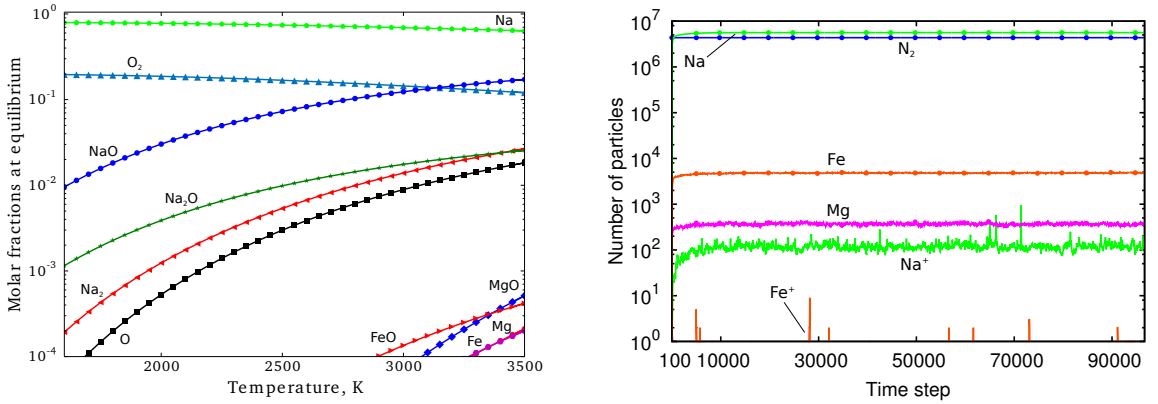

(a) (b)

Fig. 16 On the left (a), the composition of the ablated vapour in equilibrium with its condensed phase is shown for a range of temperature characteristic of meteorite melting. The results are obtained with the software MAGMA [8]. On the right (b), we show the history of the number of particles in the simulated domain at an altitude of 120 km. The number of Na particles is larger than N_2 for this condition. Free electrons mainly result from the Na ionization process.

two different classes of molecules. This effect has already been described in Section V for a non-ablating body and it was already observed by Boyd [9]. The result is that no particles are really characterized by such a temperature in the thermal sense. The scarce effect of collisions is also confirmed by the fact that the maximum value of the temperature seems insensitive to changes in the altitude: in fact, as the amount of collisions decreases, internal molecular modes become less excited and the gas starts behaving like a monatomic gas, showing only translational degrees of freedom.

At 120 km, the ablation phenomenon resembles a spherical expansion into vacuum, with the ablated vapour able to travel upstream and not interacting much with the incoming jet. In this condition, a metal cloud forms all around the body, in almost spherical symmetry. The pressure of this vapour is higher than the stagnation pressure generated by the air molecules. At 100 km, the density profile of the ablated vapour along the stagnation line is very similar to the one at 120 km, but still different in terms of molar fraction (compare Figure 17 and 18). On the other hand, at 80 km, the concentration of metals ahead of the body is less important and leads to two possible considerations. First, the vapour is taken away by the incoming jet; second, the sodium atoms are immediately scattered back towards the wall where they can condense.

From Figure 18, similar concentration of metals are visible in the trail for all the conditions. However, between 80 and 120 km, a difference of 2 or 3 orders of magnitude exist in the free electrons concentration. This suggests that hyperthermal air-vapour collisions play a significant role in this process.

At last, we perform the computation of the extended trail. In order to simulate the vapour expansion in the atmosphere with the methodology described in Section V, we employ the information at the outlet of the DSMC domain and we march along the streamlines. In this case, we use the same set of species as in the DSMC simulation, i.e. no thermochemical refinement, but we allow the electrons to recombine in agreement with the reverse rate of Reaction 30.

The evolution of radial profiles suggests a de-ionization process dominated by diffusion, whereas recombination seems not to be effective. In Figure 19, the axial and radial profiles for the free electrons obtained from our computation are shown for the 80 km test case. These profiles are seen to follow closely the analytical solution for radial diffusion (see Jones, [40]), once the proper diffusion coefficient is chosen. This confirms the importance of diffusion over chemistry in the current test case.

In [14], Baggaley suggests that "meteoric plasma is dissipated by rapid diffusion high in the atmosphere and by the effects of chemistry in the lower regions". In his findings, the loss of ionization is governed by:

$$M^+ + O_3 \rightarrow MO^+ + O_2 \tag{31}$$

and the subsequent dissociative recombination:

$$MO^+ + e^- \rightarrow M + O \tag{32}$$

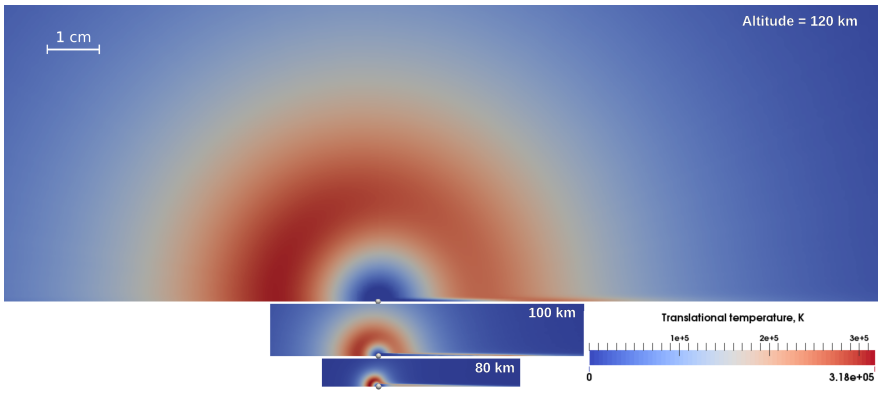

(a)

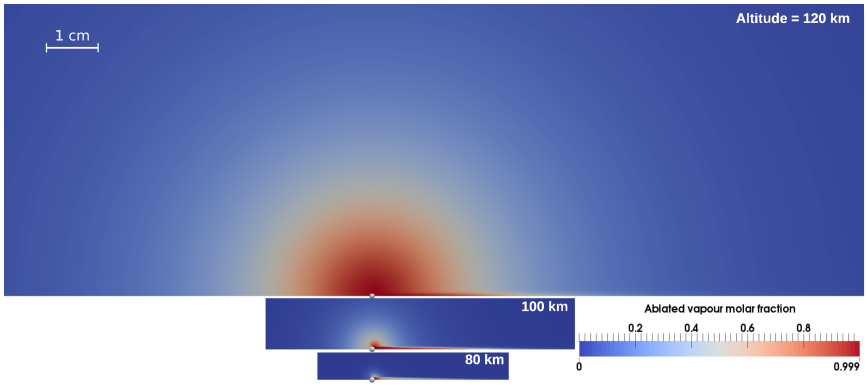

(b)

Fig. 17 Fields for the translational temperature (a) and the ablated vapour molar fraction (b) for three different altitudes of detection: 80, 100, and 120 km.

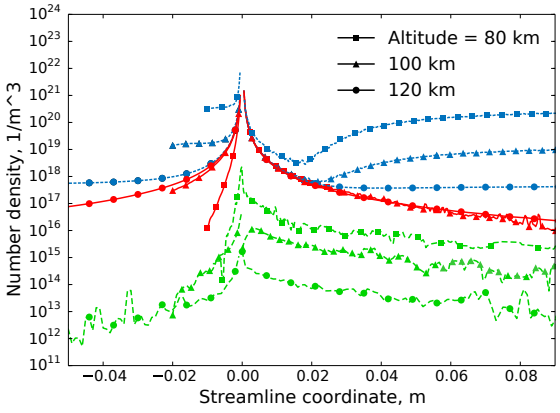

Fig. 18 Density profiles along the stagnation line for three different altitude conditions: air-vapour mixture ····, ablated vapour ——, and free electrons - - -.

However, none of these two reactions have been included in our simulations and this will be considered for future work.

In Figure 20, Na molar fraction contours reveal a trail only few centimetres wide, but several meters long. If we look at the number density profiles in Figure 21, chemical traces are present far away behind the meteoroid. At high altitude, the trail tends to diffuse much more than at lower altitude: at 100 km, Na traces are detectable in a 10 m radius cone after 1 km.

Note that all the trail plots of this paper are to be considered in a frame of reference fixed to the meteoroid. Therefore,

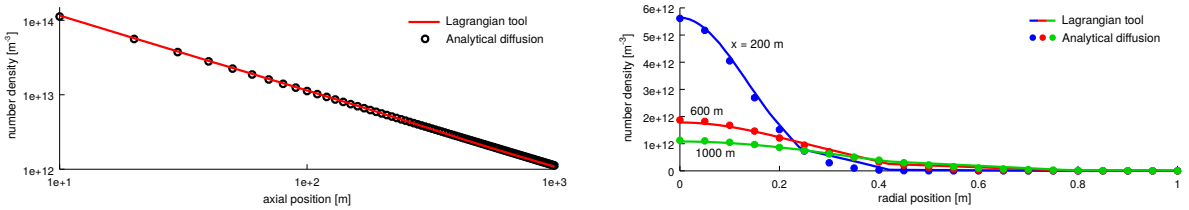

Fig. 19 Evolution of the free electrons along the trail at 80 km altitude: axial profile (a) and radial profiles at different axial positions (b). The matching with Jones' [40] analytical solution proves that the flow is dominated by diffusion.

the reported simulations are to be interpreted, by a ground based observer, as a simulation of one point of the trajectory. In fact, what an observer moving with the meteoroid sees as a trail which relaxes to the free-stream velocity and develops in space, is seen by a ground observer as the radial evolution of a trail whose velocity relaxes to zero a few diameters after the meteoroid. In this way, the given plots can be interpreted as the radial evolution in one particular position of the sky, as time passes. Free-stream density and temperature can thus be taken as constant during the radial evolution, even for long simulations.

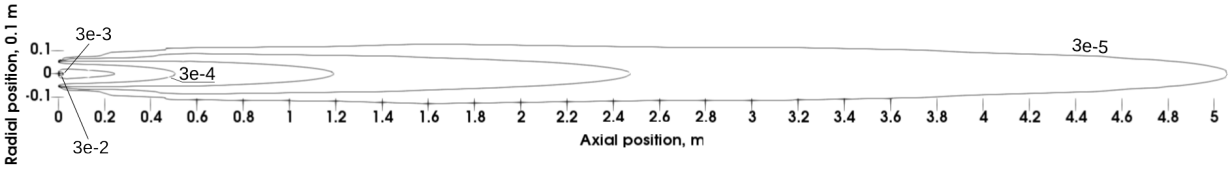

Fig. 20 Molar fraction contours for sodium vapour at 80 km altitude. The trail is only few centimetres wide, but it extends for several meters in length.

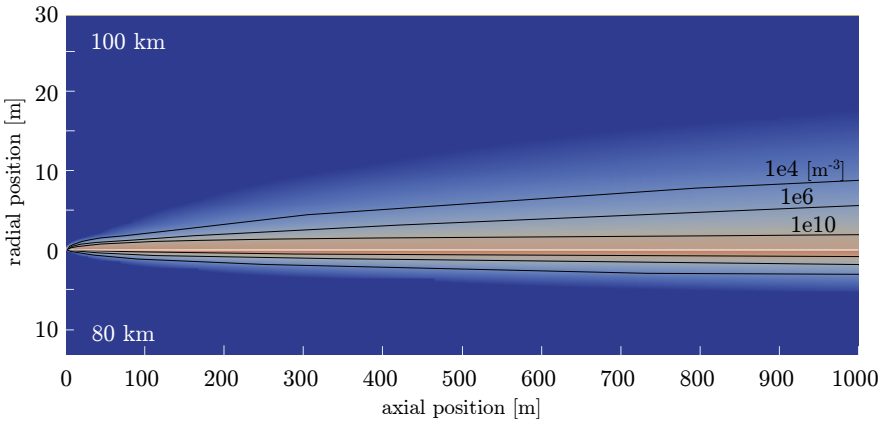

Fig. 21 Number density contours for sodium vapour in an extended diffusing trail computation. Comparison between 80 and 100 km altitudes.

VII. Conclusions

We have studied the dynamics of the vapour ejected from an ablating meteoroid, its interaction with the free-stream, and evolution in the trail. DSMC has been employed to analyse the detailed flowfield structure in the surroundings of the meteoroid. At this scope, an evaporation boundary condition has been implemented and the transport properties of the metals in the gas phase computed. We have compared predicted values of viscosity and thermal conductivity with

experimental data available in the literature for some neutral alkali species. In a second step, the evolution of the free electrons and metals in the long trail has been simulated by means of a lightweight Lagrangian reactor solver developed for the purpose.

As study case, we have chosen the flow around a 1 mm meteoroid evaporating, not far from its melting condition, at different altitudes. A high level of thermal nonequilibrium has been measured in the head of the meteor. At higher altitudes, the vapour can travel upstream without interacting much with the incoming jet. On the other hand, at higher densities, condensation seems to play a significant role in the stagnation region. Finally, a trail, several meters long and formed by metallic species, generates behind the body. Ionization of sodium turns out to be the dominant process in the production of free electrons, whereas radial diffusion seems to prevail over recombination as depletion mechanism.

Future work will be focused on the theoretical assessment of direct impact ionization cross sections to tune steric factors in the TCE model [47]. A full mechanism for the chemistry of metallic species in the mesosphere will be taken into account to reproduce the chemistry in the trail at free-stream temperatures [48]. Finally, we will try to validate the numerical modelling by comparing predicted electron concentrations with observed data from radio/radar detection.

Acknowledgements

The research presented here was funded by a PhD grant of the Research Foundation Flanders (FWO).

References

[1] Vondrak, T., Plane, J. M. C., Broadley, S., and Janches, D., "A Chemical Model of Meteoric Ablation," *Atmospheric Chemistry and Physics*, Vol. 8, No. 23, 2008, pp. 7015–7031.

[2] Josyula, E., and Burt, J., "Review of Rarefied Gas Effects in Hypersonic Applications," Tech. rep., RTO-EN-AVT-194, 2011.

[3] Lamy, H., Ranvier, S., Keyser, J. D., Gamby, E., and Calders, S., "BRAMS: the Belgian RAdio Meteor Stations," *Meteoroids Conference*, Breckenridge, CO, 2010.

[4] Ceplecha, Z., Borovicka, J., Elford, W. G., ReVelle, D. O., Hawkes, R., Porubcan, V., and Simek, M., "Meteor Phenomena and Bodies," *Space Science Reviews*, Vol. 84, No. 3, 1998, pp. 327–471.

[5] `http://brams.aeronomie.be/`, Belgian RAdio Meteor Stations (BRAMS) website.

[6] Bronshten, V. A., *Physics of Meteoric Phenomena*, D. Reidel Publishing Co., 1983.

[7] Campbell-Brown, M. D., and Koschny, D., "Model of the Ablation of Faint Meteors," *Astronomy and Astrophysics*, Vol. 418, No. 2, 2004, pp. 751–758.

[8] Fegley, B., and Cameron, A. G. W., "A Vaporization Model for Iron/Silicate Fractionation in the Mercury Protoplanet," *Earth and Planetary Science Letters*, Vol. 82, 1987, pp. 207–222.

[9] Boyd, I. D., "Computation of Atmospheric Entry Flow About a Leonid Meteoroid," *Earth, Moon and Planets*, Vol. 82, 2000, pp. 93–108.

[10] Bird, G. A., *Molecular Gas Dynamics and the Direct Simulation of Gas Flows*, Oxford University Press, 1994.

[11] Vinković, D., "Thermalization of Sputtered Particles as the Source of Diffuse Radiation from High Altitude Meteors," *Advances in Space Research*, Vol. 39, No. 4, 2007, pp. 574–582.

[12] Stokan, E., and Campbell-Brown, M. D., "A Particle-Based Model for Ablation and Wake Formation in Faint Meteors," *Monthly Notices of the Royal Astronomical Society*, Vol. 447, No. 2, 2015, pp. 1580–1597.

[13] Gallis, M. A., Torczynski, J. R., Plimpton, S. J., Rader, D. J., and Koehler, T., "Direct Simulation Monte Carlo: The Quest for Speed," *AIP Conference Proceedings*, Vol. 1628, No. 1, 2014, pp. 27–36.

[14] Murad, E., and Williams, I., *Meteors in the Earth's Atmosphere*, Cambridge University Press, 2002.

[15] Popova, O. P., Sidneva, S. N., Shuvalov, V. V., and Strelkov, A. S., *Screening of Meteoroids by Ablation Vapor in High-Velocity Meteors*, Springer Netherlands, 2000, pp. 109–128.

[16] Bonacina, C., Comini, G., Fasano, A., and Primicerio, M., "Numerical Solution of Phase-Change Problems," *International Journal of Heat and Mass Transfer*, Vol. 16, No. 10, 1973, pp. 1825–1832.

[17] Dias, B., Bariselli, F., Turchi, A., Frezzotti, A., Chatelain, P., and Magin, T. E., "Development of a Melting Model for Meteors," *30th International Symposium on Rarefied Gas Dynamics*, Victoria, BC, 2016.

[18] Carslaw, H. S., and Jaeger, J. C., *Conduction of Heat in Solids*, Oxford at the Clarendon Press, 1959.

[19] `https://www.imo.net/resources/databases/`, International Meteor Organization (IMO) website.

[20] Loehle, S., Zander, F., Hermann, T., Eberhart, M., Meindl, A., Oefele, R., Vaubaillon, J., Colas, F., Vernazza, P., Drouard, A., and Gattacceca, J., "Experimental Simulation of Meteorite Ablation during Earth Entry using a Plasma Wind Tunnel," *The Astrophysical Journal*, Vol. 837, No. 2, 2017, p. 112.

[21] Ferziger, J. H., and Kaper, H. G., *Mathematical Theory of Transport Processes in Gases*, Elsevier Science Publishing, 1972.

[22] Frezzotti, A., "Boundary Conditions at the Vapor-Liquid Interface," *Physics of Fluids*, Vol. 23, No. 3, 2011, p. 030609.

[23] Schaefer, L., and Fegley, B., "A Thermodynamic Model of High Temperature Lava Vaporization on Io," *Icarus*, Vol. 169, No. 1, 2004, pp. 216–241.

[24] Cercignani, C., *Mathematical Methods in Kinetic Theory*, Plenum Press, New York, 1969.

[25] Ghatee, M. H., and Niroomand-Hosseini, F., "Hard-Wall Potential Function for Transport Properties of Alkali Metal Vapors," *The Journal of Chemical Physics*, Vol. 126, No. 1, 2007, p. 014302.

[26] Bird, R. B., Stewart, W. E., and Lightfoot, E. N., *Transport Phenomena*, John Wiley and Sons, 1960.

[27] Svehla, R., "Estimated Viscosities and Thermal Conductivities of Gases at High Temperatures," Tech. rep., NASA-TR-R-132, 1962.

[28] McGee, B. C., Hobbs, M. L., and Baer, M. R., "Exponential 6 Parameterization for the JCZ3-EOS," Tech. rep., SAND98-1191, 1998.

[29] Lee, D., and Bonilla, C. F., "The Viscosity of the Alkali Metal Vapors," *Nuclear Engineering and Design*, Vol. 7, No. 5, 1968, pp. 455 – 469.

[30] Vargaftik, N. B., Vinogradov, Y. K., Dolgov, V. I., Dzis, V. G., Stepanenko, I. F., Yakimovich, Y. K., and Yargin, V. S., "Viscosity and Thermal Conductivity of Alkali Metal Vapors at Temperatures up to 2000 K," *International Journal of Thermophysics*, Vol. 12, No. 1, 1991, pp. 85–103.

[31] Briggs, D. E., "Thermal Conductivity of Potassium Vapor," Ph.D. thesis, 1968.

[32] Stefano, D. I., Timorot, D., and Totski, Y. Y., "Viscosity and Thermal Conductivity of the Vapors of Sodium and Potassium," *High Temperature Thermophys.*, Vol. 4, 1966, p. 131.

[33] Ivanov, M. S., Markelov, G. N., Gimelshein, S. F., Mishina, L. V., Krylov, A. N., and Grechko, N. V., "High-Altitude Capsule Aerodynamics with Real Gas Effects," *Journal of Spacecraft and Rockets*, Vol. 35, No. 1, 1998, pp. 16–22.

[34] LeBeau, G. J., "A Parallel Implementation of the Direct Simulation Monte Carlo Method," *Computer Methods in Applied Mechanics and Engineering*, Vol. 174, No. 3-4, 1999, pp. 319–337.

[35] Park, C., Jaffe, R. L., and Partridge, H., "Chemical-Kinetic Parameters of Hyperbolic Earth Entry," *Journal of Thermophysics and Heat Transfer*, Vol. 15, No. 1, 2001, pp. 76–90.

[36] Carlsona, A. B., and Hassan, H. A., "Direct Simulation of Re-Entry Flows with Ionization," *Journal of Thermophysics and Heat Transfer*, Vol. 6, No. 3, 1992, pp. 400–404.

[37] Boyd, I. D., "Monte Carlo Simulation of Nonequilibrium Flow in a Low-Power Hydrogen Arcjet," *Physics of Fluids*, Vol. 9, No. 10, 1997, pp. 3086–3095.

[38] Swaminathan-Gopalan, K., and Stephani, K. A., "Calibration of DSMC Parameters for Transport Processes in Ionized Air Mixtures," *45th AIAA Thermophysics Conference*, Dallas, TX, 2015.

[39] Baggaley, W., "The De-Ionization of Dense Meteor Trains," *Planetary and Space Science*, Vol. 26, No. 10, 1978, pp. 979–981.

[40] Jones, W., and Jones, J., "Ionic Diffusion in Meteor Trains," *Journal of Atmospheric and Terrestrial Physics*, Vol. 52, No. 3, 1990, pp. 185–191.

[41] Lee, J.-H., "Basic Governing Equations for the Flight Regimes of Aeroassisted Orbital Transfer Vehicles," *Thermal Design of Aeroassisted Orbital Transfer Vehicles*, Vol. 96, 1985, pp. 3–53.

[42] Anderson, J. D., *Hypersonic and High Temperature Gas Dynamics*, Aiaa, 2000.

[43] Giovangigli, V., *Multicomponent Flow Modeling. Modeling and Simulation in Science, Engineering and Technology*, Birkhäuser Boston Inc., Boston, MA, 1999.

[44] Boccelli, S., "Development of a Lagrangian Solver for Thermochemical Nonequilibrium Flows," Master's thesis, 2016.

[45] Scoggins, J., and Magin, T. E., "Development of Mutation++: Multicomponent Thermodynamic and Transport Properties for Ionized Plasmas written in C++," *11th AIAA/ASME Joint Thermophysics and Heat Transfer Conference*, Atlanta, GA, 2014.

[46] Dressler, R. A., *Chemical Dynamics in Extreme Environments*, World Scientific, Advanced Series in Physical Chemistry - Vol. 11, 2001.

[47] Kunc, J. A., and Soon, W. H., "Analytical Ionization Cross Sections for Atomic Collisions," *The Journal of Chemical Physics*, Vol. 95, No. 8, 1991, pp. 5738–5751.

[48] Plane, J. M. C., Feng, W., and Dawkins, E. C. M., "The Mesosphere and Metals: Chemistry and Changes," *Chemical Reviews*, Vol. 115, No. 10, 2015, pp. 4497–4541.